

Dislocation and twin substructure evolution during strain hardening of an Fe–22 wt.% Mn–0.6 wt.% C TWIP steel observed by electron channeling contrast imaging

I. Gutierrez-Urrutia*, D. Raabe

Max-Planck-Institut für Eisenforschung, Max-Planck Str. 1, D-40237 Düsseldorf, Germany

Received 11 March 2011; received in revised form 3 July 2011; accepted 4 July 2011

Available online 29 July 2011

Abstract

We study the kinetics of the substructure evolution and its correspondence to the strain hardening evolution of an Fe–22 wt.% Mn–0.6 wt.% C TWIP steel during tensile deformation by means of electron channeling contrast imaging (ECCI) combined with electron backscatter diffraction (EBSD). The contribution of twin and dislocation substructures to strain hardening is evaluated in terms of a dislocation mean free path approach involving several microstructure parameters, such as the characteristic average twin spacing and the dislocation substructure size. The analysis reveals that at the early stages of deformation (strain below 0.1 true strain) the dislocation substructure provides a high strain hardening rate with hardening coefficients of about $G/40$ (G is the shear modulus). At intermediate strains (below 0.3 true strain), the dislocation mean free path refinement due to deformation twinning results in a high strain rate with a hardening coefficient of about $G/30$. Finally, at high strains (above 0.4 true strain), the limited further refinement of the dislocation and twin substructures reduces the capability for trapping more dislocations inside the microstructure and, hence, the strain hardening decreases. Grains forming dislocation cells develop a self-organized and dynamically refined dislocation cell structure which follows the similitude principle but with a smaller similitude constant than that found in medium to high stacking fault energy alloys. We attribute this difference to the influence of the stacking fault energy on the mechanism of cell formation.

© 2011 Acta Materialia Inc. Published by Elsevier Ltd. All rights reserved.

Keywords: Strain hardening; Electron channeling contrast imaging; Austenitic steel; Dislocation structures; Deformation twinning

1. Introduction

High-manganese steels have received much interest in recent years due to their outstanding mechanical properties combining high strength and ductility. This property profile is attributed to their high strain hardening capacity. High-manganese steels are typically austenitic steels, i.e. face-centered cubic (fcc) alloys, with a high Mn content (above 20% wt.%) and additions of elements such as carbon (<1 wt.%), silicon (<3 wt.%) and aluminum (<10 wt.%). This steel grade exhibit different hardening mechanisms, such as transformation-induced plasticity

(TRIP) [1,2], twinning-induced plasticity (TWIP) [1,3–8] or microband-induced plasticity (MBIP) [9,10]. The activation of these mechanisms is strongly dependent on the stacking fault energy. TRIP is observed in very low stacking fault steels (below 20 mJ m^{-2}) and is associated with the transformation of austenite (fcc phase) into ϵ -martensite (hexagonal close-packed phase), which in turn further acts as nucleus of α' -martensite (body-centered cubic or tetragonal phase) [11,12]. TWIP is observed in medium stacking fault energy steels ($20\text{--}40 \text{ mJ m}^{-2}$) and is characterized by the formation of deformation twins with nanometer thickness. MBIP has been recently reported in steel grades with high stacking fault energy ($\sim 90 \text{ mJ m}^{-2}$) and is attributed to the formation of microbands, which are in-grain shear zones that are confined by geometrically nec-

* Corresponding author. Tel.: +49 2116792 211; fax: +49 2115792333.
E-mail address: i.gutierrez@mpie.de (I. Gutierrez-Urrutia).

essary boundaries or conventional grain boundaries. These microstructure features (ϵ -martensite plates, deformation twins and microbands) lead to a remarkable variety of strain hardening phenomena as they all act as effective obstacles for dislocation glide. High-manganese TWIP steels are characterized by a hierarchical microstructure refinement that includes complex dislocation and twin substructures, and their interactions. Although there are some previous studies on the strain hardening behavior in TWIP steels, the details of the underlying kinetics of the substructure evolution and its correspondence to the stress–strain and strain hardening evolution is not yet fully understood. Most of these works analyze strain hardening in terms of a dislocation mean free path (MFP) approach, focusing essentially on a single microstructure parameter, namely, the twin spacing [3,13–17]. These works attribute the high strain hardening rate at intermediate strains (0.1–0.2 true strain) to twin spacing refinement. The increasing density of deformation twin boundaries and the strong effect they have on dislocation glide leads to the so-called “dynamic Hall–Petch effect”. However, our analysis reveals that the deformed microstructure of these alloys is too complicated to be reduced to a single microstructure parameter and, therefore, a detailed analysis of the contribution of dislocation and twin substructures, as well as their interactions, to strain hardening is required.

One important limitation in the characterization of TWIP steels is the complexity of the microstructure, which involves features of different length scales: deformation twins with thicknesses of some tens of nanometers [3,16,18] and dislocation substructures extending over several micrometers. As a consequence of this scale discrepancy, quantitative microstructure characterization by conventional electron microscopy techniques such as electron backscatter diffraction (EBSD) or transmission electron microscopy (TEM) is limited due to the angular resolution (EBSD) and the small field of view (TEM), respectively. In this study, therefore, we make use of electron channeling contrast imaging (ECCI), which is conducted in a scanning electron microscope (SEM), to perform a quantitative characterization of the deformation microstructure of TWIP steel. The ECCI technique has been established as an excellent tool for examining complex deformation microstructures of metallic materials, revealing microstructure features such as deformation twins, stacking faults and complex dislocation arrangements from a wide field of view directly in the SEM [6,19–25]. The reason for the recent improvement in the ECCI technique lies in its combination with EBSD. This allows us to efficiently identify optimum contrast conditions and, therefore, produce ECCI images of crystal defects under controlled diffraction conditions [24].

The present study aims at understanding the strain hardening behavior of an Fe22 wt.% Mn–0.6 wt.% C TWIP steel through a complete quantitative characterization of the dislocation and twin substructure evolution via an EBSD-optimized ECCI approach. The contribution of

the so-characterized substructure to the strain hardening is analyzed in terms of the dislocation mean free path approach involving several microstructure parameters, such as the characteristic average twin spacing and the dislocation substructure length scale.

2. Experimental

The TWIP steel used in this study had the chemical composition Fe–22 wt.% Mn–0.6 wt.% C. The material was melted in an induction furnace under an Ar atmosphere and cast into round bars of 25 mm diameter. To avoid Mn segregation [26], samples were swaged to 20% area reduction at 1000 °C and subsequently solution-treated for 4 h at 1100 °C under Ar. Thereafter, samples were hot-rolled to 75% engineering thickness at 1000 °C followed by air cooling. The hot-rolled material showed a fully austenitic structure with an average grain size of 50 μm , which remained stable during deformation at room temperature.

Tensile tests were carried out at room temperature at an initial strain rate of $5 \times 10^{-4} \text{ s}^{-1}$. In addition to tensile testing to failure, interrupted tensile tests to true strains of $\epsilon = 0.05, 0.10, 0.30$ and 0.40 were performed to study the microstructural evolution as a function of strain. The tensile bone-shaped samples had an 8 mm gage length, 2 mm gage width and 1 mm gage thickness. The monotonic tensile deformation experiments were carried out on a tensile test instrument (Kammrath & Weiss GmbH, Dortmund, Germany) equipped with a digital image correlation (DIC) system (ARAMIS system, GOM-Gesellschaft für Optische Messtechnik mbH, 38106 Braunschweig, Germany) to measure the local and macroscopic strain distribution. Details of this set-up are described in Ref. [27]. The surface pattern required for DIC was obtained as explained in Ref. [6]. Averaged engineering strain values were retrieved from the corresponding strain maps and used to calculate the true stress–strain values.

Microstructures of the tensile deformed TWIP steel were examined by two types of scanning electron microscopy techniques, namely, electron back scatter diffraction (EBSD) and electron channeling contrast imaging (ECCI). The EBSD technique was used to analyze the local crystallographic texture together with the dislocation and twin substructure. Orientation maps were taken in a 6500 F JEOL field emission gun-scanning electron microscope equipped with a TSL OIM EBSD system at 15 kV acceleration voltage and with a working distance of 15 mm. EBSD maps are displayed as inverse pole figure (IPF) maps in the direction of the tensile axis (TA). The ECCI technique was used to image deformation twins and dislocation substructures, as introduced in a previous work on TWIP steels [6]. A recently reported new set-up for ECCI [24] was used in this study to obtain ECCI images under controlled diffraction conditions, enabling an enhanced dislocation and interface contrast. The set-up makes use of the EBSD technique for orienting the crystal into optimal diffraction con-

ditions. ECCI images were obtained with optimum contrast by orienting the matrix crystal exactly in the Bragg condition for a high-intensity reflection and exciting the corresponding diffraction vector in a “two-beam” condition. ECCI observations were carried out in a Zeiss Cross-beam instrument (XB 1540; Carl Zeiss SMT AG, Germany) consisting of a Gemini-type field emission gun electron column and a focused ion beam device (Orsay Physics). ECCI was performed at 10 kV acceleration voltage and a working distance of 6 mm, using a solid-state four-quadrant BSE detector. The microscope was run in the “high current” mode and an objective lens aperture of 120 μm was used.

3. Results

3.1. Strain hardening

Fig. 1 shows a set of true stress–strain curves of the Fe–22 wt.% Mn–0.6 wt.% C TWIP steel tensile deformed at a strain rate of $5 \times 10^{-4} \text{ s}^{-1}$. We include here both the complete and interrupted tensile tests. The TWIP steel exhibits excellent mechanical properties, combining high strength (ultimate tensile strength of 1.1 GPa) and ductility (elongation to failure of 50%). It is important to note that between 0.1 and 0.2 true strain the stress–strain curve assumes a slightly concave shape, i.e. at this strain level secondary strain hardening effects seem to occur.

Fig. 2 shows the normalized strain hardening rate (normalized by the shear modulus) vs. flow stress (a) and true strain (b) of the tensile deformed material. Arrows indicate the different deformation stages described in the subsequent section. The main features revealed in Fig. 2 are, first, the remarkably high overall strain hardening rate and, second, the fact that the curve reveals a minimum at intermediate strains (0.06–0.1 true strain). This hardening

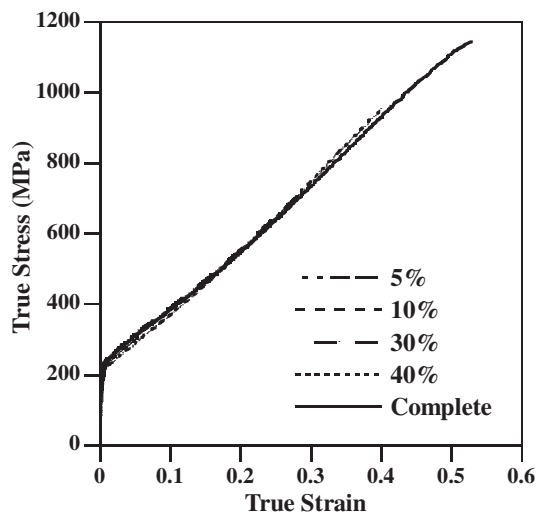


Fig. 1. True stress–true strain curves of Fe–22 wt.% Mn–0.6 wt.% C TWIP steel corresponding to interrupted and complete (i.e. until rupture) tensile tests. Initial strain rate: $5 \times 10^{-4} \text{ s}^{-1}$.

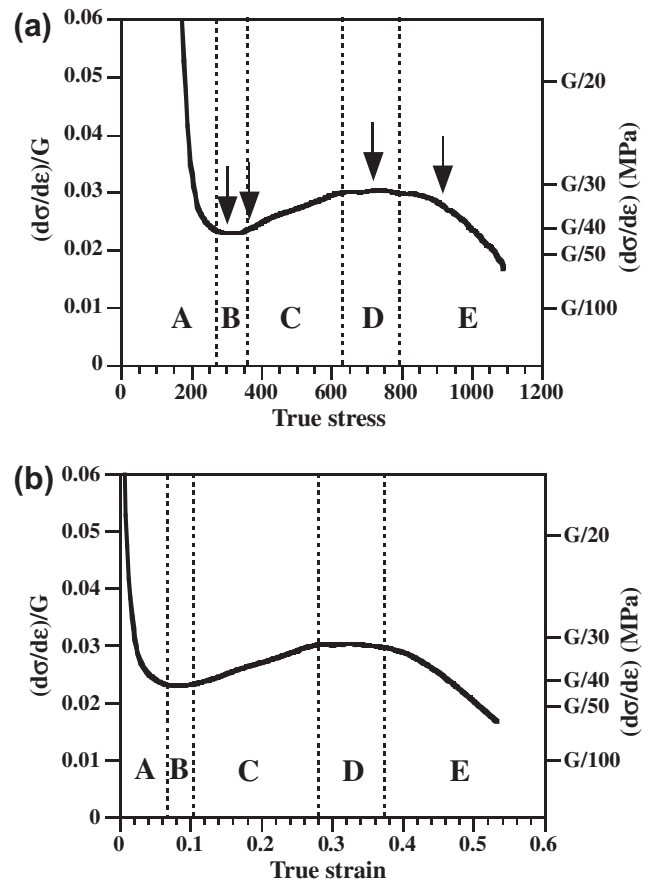


Fig. 2. Normalized strain hardening rate (normalized by the shear modulus) vs. true stress (a) and true strain (b) of tensile deformed Fe–22 wt.% Mn–0.6 wt.% C TWIP steel.

stage is followed by a high strain hardening rate at higher deformations. Typically, structural metallic alloys reveal a monotonous decay of the strain hardening rate as a function of strain. More specifically, in the current study five different deformation stages can be clearly distinguished in the evolution of the strain hardening rate with the true stress. The first stage, referred to as stage A, is characterized by a continuous decrease in the strain hardening rate until 270 MPa. This stage is similar to the stage III hardening regime of fcc metals with high stacking fault energy, such as copper and aluminum [28]. At this stress level, the strain hardening coefficient is about $G/40$, where G is the shear modulus. The hardening rate remains almost constant with a strain hardening coefficient of about $G/40$ during a small stress increment until 360 MPa (stage B). With increasing stress, the strain hardening rate increases gradually, reaching a strain hardening coefficient of about $G/30$ at 630 MPa (stage C). With further stress, the strain hardening rate is nearly constant, with a strain hardening coefficient of about $G/30$ up to a stress level of 800 MPa (stage D). Finally, the strain hardening rate decreases until rupture (stage E). It should be pointed out that the labeling of the hardening stages used in this work must not be confused with the classical hardening stage analysis used for

single crystals and polycrystals, which does not reveal a minimum in strain hardening after the classical stage III hardening regime.

3.2. Texture evolution

In its initial hot-rolled and homogenized state the material showed a fully austenitic structure, which remained stable during deformation at room temperature. No evidence of ϵ -martensite was detected by EBSD on the tensile deformed samples. Fig. 3 shows the texture evolution of the TWIP steel during tensile deformation. Fig. 3a shows the IPF for the crystal direction along the TA of the initial material, revealing a weak texture before the tensile test. Fig. 3b–e shows the textures in terms of TA-IPFs of the steel deformed to 0.05, 0.10, 0.30 and 0.40 true strain, respectively. We observe that the texture sharpens slightly during tensile deformation. At 0.3 true strain, the texture is characterized by two strong components, namely $\langle 111 \rangle // \text{TA}$ and $\langle 001 \rangle // \text{TA}$, which both remain stable

and sharpen slightly further during the ongoing deformation. Similar textures have been previously observed in tensile deformed TWIP steels at room temperature [16,29].

3.3. Evolution of the dislocation and twin substructure

At the early stage of deformation (strain below a true strain of 0.1), the microstructure mainly consists of dislocation substructures, with very few deformation twins. In this regime, the twinned area fraction is about 0.001 (Fig. 4a and b). Parts (a) and (b) of the figure show ECCI images of deformed microstructures of TWIP steels at 0.05 true strain/310 MPa and 0.1 true strain/380 MPa, respectively. These stress levels fall into stage B of strain hardening. The micrographs reveal that less than 20% of all grains contain deformation twins, which are mainly distributed along a single active twinning system (the primary twin system). At this stage of deformation, planar arrangements of dislocations consisting of dense dislocation layers forming on planes corresponding to the most active slip systems

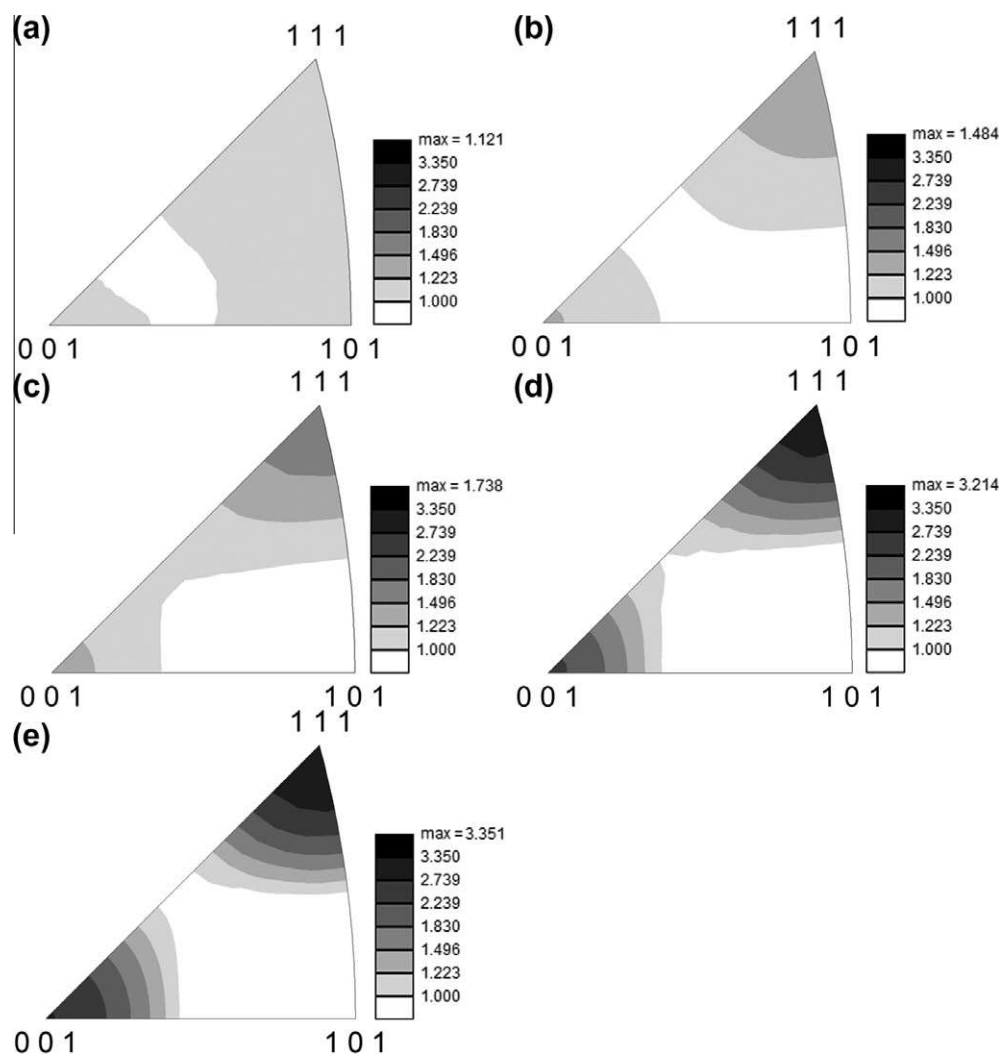


Fig. 3. IPFs along the TA direction of Fe–22 wt.% Mn–0.6 wt.% C TWIP steel in different states: as hot-rolled (a); tensile deformed to 0.05 true strain (b); 0.1 true strain (c); 0.3 true strain (d); 0.4 true strain (e).

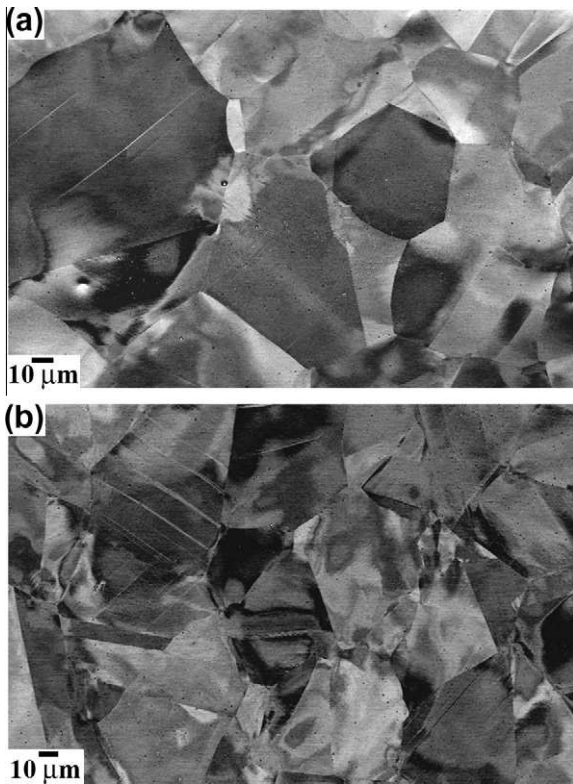


Fig. 4. ECCI images of deformed microstructures at 0.05 true strain (a) and 0.1 true strain (b), respectively.

are visible, as illustrated in the ECCI image in Fig. 5a. These dislocation substructures are referred to as highly dense dislocation walls (HDDWs) [30–32]. HDDWs are dislocation boundaries with a high dislocation density and a rotational component separating regions with different combinations of simultaneously operating glide systems. HDDWs appear in the ECCI images under the corresponding Bragg condition as bright straight compact layers penetrating the whole grain. This dislocation pattern is similar to that obtained in bright-field TEM images of HDDWs in medium-to-high stacking fault energy metals [30,31]. However, the contrast in ECCI imaging is reverted compared to that obtained in bright-field TEM due to the electron channeling mechanism and the diffraction conditions used to image dislocation substructures. In particular, Fig. 5a shows an example of HDDWs formed along the $(-1\ 1\ -1)$ slip plane on a sample that was tensile deformed to 0.05 true strain. The ECCI-based slip trace analysis was conducted by an accompanying EBSD map in the same area. HDDWs have been observed in medium-to-high stacking fault energy metals [30,31] as well as in low stacking fault energy alloys [33,34].

With further straining (to 0.1 true strain), a heterogeneous dislocation substructure is formed due to the multiple character of slip (planar and wavy), as illustrated in Fig. 5b. Planar slip promotes the formation of structures created by the intersection of HDDWs on two different slip planes, referred to as HDDW structures. These intersec-

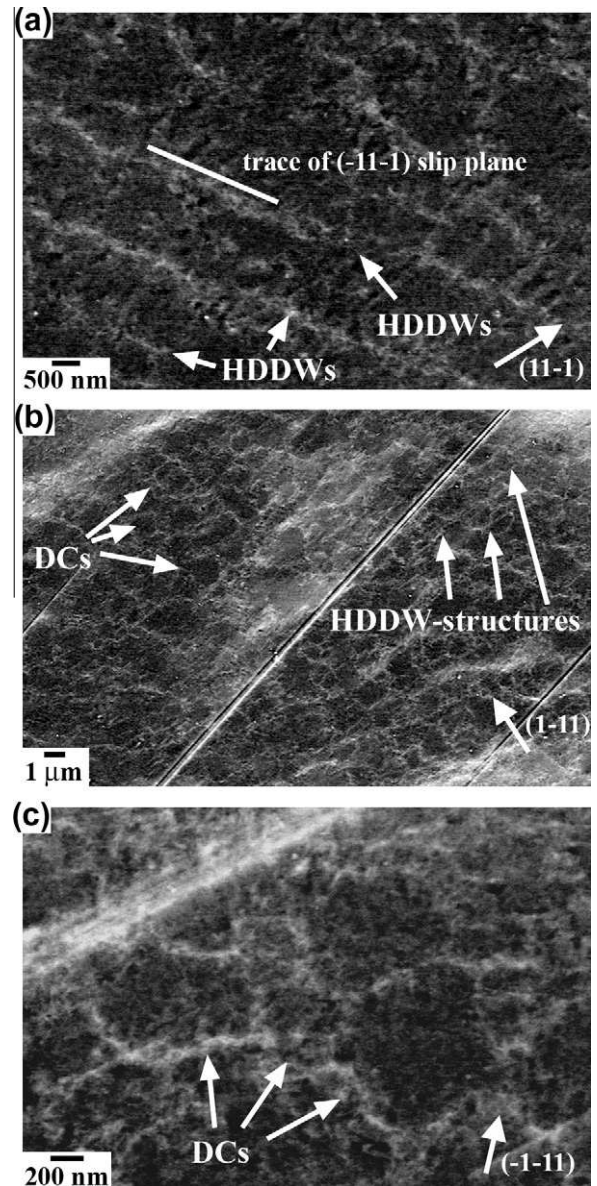


Fig. 5. ECCI images of deformed microstructure at the early stages of deformation (strain below 0.1 true strain). (a) HDDWs along the $(-1\ 1\ -1)$ slip plane on a sample tensile deformed to 0.05 true strain. The ECCI image was obtained by orienting the grain into Bragg condition using the $(1\ 1\ -1)g$ vector (arrow). (b) DCs and HDDW structures in a sample tensile deformed to 0.1 true strain. The ECCI image was obtained by orienting the grain into Bragg condition using the $(1\ -1\ 1)g$ vector (arrow). (c) Details of the DC structure on a sample tensile deformed to 0.05 true strain. The ECCI image was obtained by orienting the grain into Bragg condition using the $(-1\ -1\ 1)g$ vector (arrow).

tions lead to a checkerboard-type pattern, which is commonly observed in low stacking fault energy metals [33,34]. Wavy slip promotes the formation of equiaxed dislocation cells (DCs) similar to those observed in medium-to-high stacking fault energy metals [30,32]. These dislocation substructures appear in ECCI images under the current diffraction conditions as bright globular structures with a sharp boundary contrast. This dislocation pattern is similar to that obtained in bright-field TEM, as shown

in a previous work [24]. As discussed before, the contrast in ECCI is reverted to that in bright-field TEM due to the electron channeling mechanism and the diffraction conditions used to image dislocation substructures. The ECCI image shown in Fig. 5c reveals in detail dislocation cells with sizes ranging between 500 and 1000 nm formed at 0.05 true strain. At this strain, the average size of the dislocation substructure (both HDDW structures and DCs) is 750 nm. With further strain (0.1 true strain), the dislocation substructure is refined to an average size of 650 nm.

At a true strain of 0.3, the twinning activity increases remarkably, leading to the development of a well-defined twin substructure. At this stage, most of the grains contain deformation twins that are active in several systems (up to three twinning systems in the same grain are observed), and only around 10% of the grains are free of deformation twins. With further straining, the twin activity increases slightly. Fig. 6a and b shows ECCI images of the twin substructure formed at 0.3 true strain/720 MPa (stage D of strain hardening) and 0.4 true strain/920 MPa (stage E of strain hardening), respectively. These images show the formation of a well-defined twin substructure that penetrates the grains and subgrains. These crystals have sizes in the range between 10 and 40 μm . It can be also seen that even at high strains some grain regions remain free of deformation twins. At this stage (0.3–0.4 true strain), we can systematically distinguish three types of grains/subgrains according to the twin substructure occurring in them: type

I grains, which are characterized by a low deformation twinning activity; type II grains, which contain a well-developed twin substructure along one active twinning system (the primary twin system according to the highest Schmid factor); and type III grains, which build up a well-developed twin substructure along more than one active twinning system (primary and secondary twin systems). We define primary twin systems as those systems with the highest Schmid factor. The other twin systems are referred to as secondary twin systems. The evolution of the grain area fraction, the average size of dislocation substructures and the average twin spacing of each type of grain are shown in Table 1.

3.4. Orientation dependence of the dislocation and twin substructure

The grain orientation dependence of the twin substructure was analyzed via EBSD mapping in 150 individual grains/subgrains of a sample tensile deformed to 0.3 true strain. About 10 regions were characterized for each grain/subgrain. The average orientation is plotted in the TA-IPF of Fig. 7, with red, green and blue dots corresponding to type I, II and III grains, respectively. The data reveal that the different types of twin substructures observed are characteristic of specific orientation components: type I grains (low twinning activity) are oriented close to $\langle 001 \rangle // \text{TA}$ directions within an angular range of approximately 15° ; type II grains (primary twin system active) are oriented along the line between $\langle 001 \rangle // \text{TA}$ and $\langle 111 \rangle // \text{TA}$ directions; and type III grains (primary and secondary twin systems active) are oriented close to $\langle 111 \rangle // \text{TA}$ directions within an angular range of approximately 15° .

Figs. 8–10 show ECCI images of type I, II and III grains, respectively. Type I grains occur less frequently with an area fraction of about 10%. These grains/subgrains are oriented close to $\langle 001 \rangle // \text{TA}$ directions and exhibit low deformation twinning activity, as is evident from the small amount of twin bundles (Fig. 8a). These bundles are nucleated at grain boundaries and do not extend further up to the opposite grain boundary, but they only grow a few microns into the grain interior without impinging on other interfaces. Type I grains contain a fine equiaxed dislocation cell structure, with an average cell size of 220 nm at 0.3 true strain (Fig. 8b). Further straining (0.4 true strain) leads to a slight refinement of the cell size to an average value of 180 nm. Type II grains, with an area fraction of about 30%, exhibit significant deformation twinning activity. These grains/subgrains are oriented along the line between the $\langle 001 \rangle // \text{TA}$ and $\langle 111 \rangle // \text{TA}$ crystallographic directions. They contain a lamellar twin structure along a primary twinning system, as shown in Fig. 9a. At 0.3 true strain, the average twin spacing is 320 ± 50 nm, which is slightly reduced to 280 ± 50 nm with increasing deformation to 0.4 true strain. Fig. 9b shows that the lamellar twin structure is formed by single deformation twins, with a

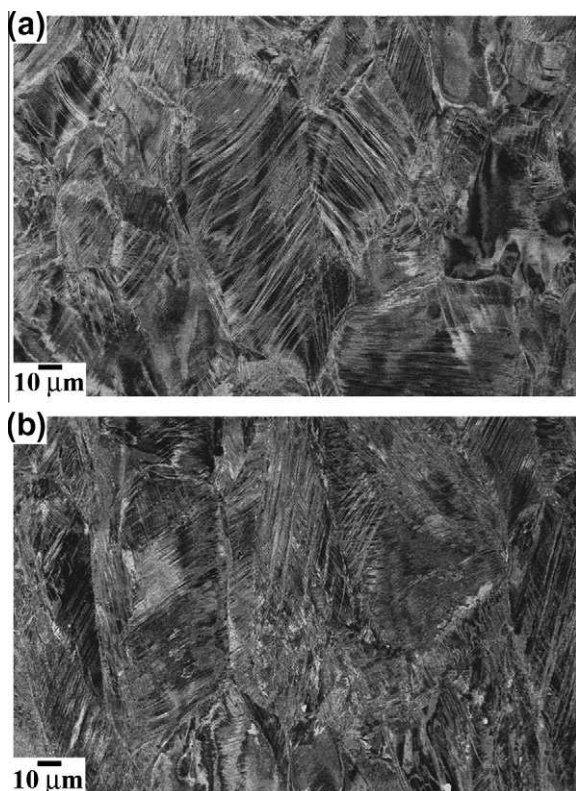


Fig. 6. ECCI images of deformation microstructures at 0.3 true strain (a) and 0.4 true strain (b), respectively.

Table 1

Evolution of the grain area fraction, the average size of dislocation substructures, and the average twin spacing with true strain/stress in type I, II and III grains. Type I grains: equiaxed cell structure with a low deformation twinning activity; type II grains: well-developed twin substructure along one active twinning system (primary twin system); type III grains: dislocation cells and highly-dense dislocation walls-structures with a well-developed twin substructure along more than one active twinning system (primary and secondary twin systems) (see also Figs. 7 and 15).

True strain	True stress (MPa)	Type I		Type II		Type III		
		Area fraction (%)	Dislocation substructure size (nm)	Area fraction (%)	Twin spacing (nm)	Area fraction (%)	Twin spacing (nm)	Dislocation substructure size (nm)
0.05	310	100	750 ± 150	0	–	0	–	–
0.1	380	~100	650 ± 100	0	–	0	–	–
0.3	720	10	220 ± 50	30	320 ± 50	60	430 ± 100	550 ± 100
0.4	920	10	180 ± 50	30	280 ± 50	60	260 ± 50	450 ± 100

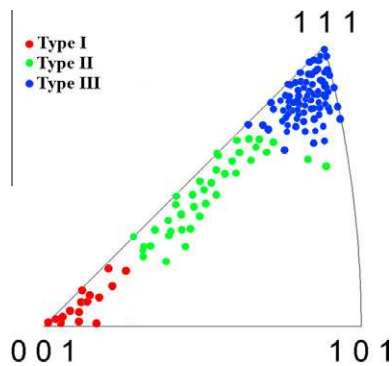


Fig. 7. IPFs along the TA direction showing experimental grain orientations of a sample deformed to 0.3 true strain with red, green and blue dots corresponding to type I, II and III grains, respectively. The classification indicates basic differences in the dislocation cell and twinning substructures developed in the different grains: type I grains: equiaxed cell structure with a low deformation twinning activity; type II grains: well-developed twin substructure mainly along one active twinning system (primary twin system: system with highest Schmid factor); type III grains: DCs and HDDW structures with a well-developed twin substructure along more than one active twinning system (primary and secondary twin systems) (see also Fig. 15 and Table 1).

thickness distribution ranging from 30 to 100 nm. At 0.3–0.4 true strain, the average twin thickness is 80 ± 20 nm. True twin thicknesses and spacings were determined by ECCI observations at high magnification for a set of about 500 deformation twins under diffraction conditions with a $\{111\}$ plane reflector parallel to the twin interface, i.e. the twins were monitored in edge-on position. Fig. 9a and b reveals that twin boundaries cut through the existing dislocation substructure developed during the early stages of deformation (HDDW structures and DCs) without experiencing strong resistance. As a consequence, a new block-shaped nanostructure is formed, as revealed in Fig. 9b. This nanostructure consists of twin boundaries along the active twin system and dislocation walls (HDDWs or cell walls) formed along the most active slip systems. The average size of the blocky nanostructure can be roughly estimated as the twin spacing times the cell size,

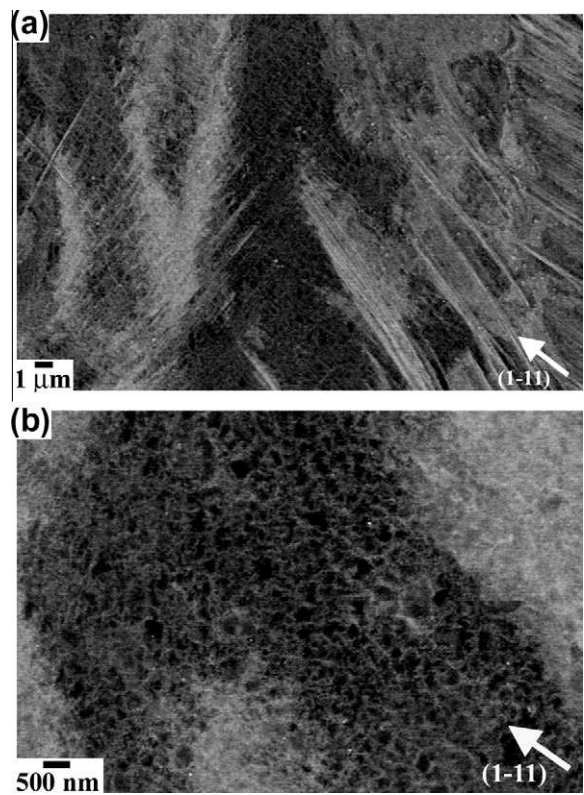


Fig. 8. ECCI images of deformation microstructure of a type I grain at 0.3 true strain. ECCI images were obtained by orienting the grain into Bragg condition using the $(1-11)g$ vector (arrow). (a) Large field of view image showing dislocation cells and bundles of twins. (b) Details of the dislocation cell structure.

which is about $300 \text{ nm} \times 500 \text{ nm}$ in the 0.3–0.4 true strain regime. Type III grains are the most frequently occurring grains, with an area fraction of 60%. These grains are oriented close to $\langle 111 \rangle // \text{TA}$ directions and exhibit a significant deformation twinning and dislocation activity. The twinning activity results in a well-defined twin substructure consisting of a primary twin system and one or two secondary twin systems (Fig. 10a). Deformation twins are typically arranged in bundles with thicknesses between 80 and 450 nm. Thin deformation twins with a thickness

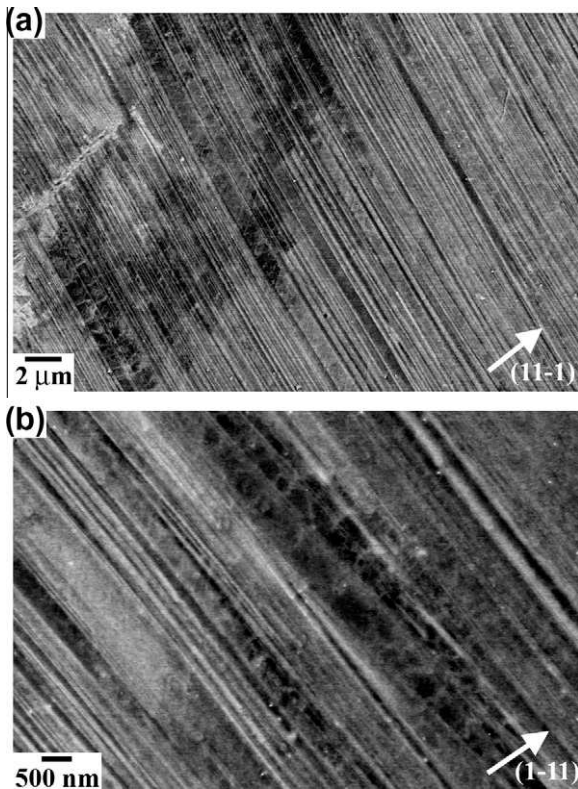


Fig. 9. ECCI images of deformation microstructure of a type II grain at 0.3 true strain. (a) Large field of view image showing a lamellar twin structure. The ECCI image was obtained by orienting the grain into Bragg condition using the $(1\ 1\ -1)g$ vector (arrow). (b) Details of the lamellar twin structure. Dislocation boundaries are visible in areas with large twin spacing. The ECCI image was obtained by orienting the grain into Bragg condition using the $(1\ -1\ 1)g$ vector (arrow).

between 20 and 60 nm are only observed on secondary twin systems, as illustrated in Fig. 10b. Apparent twin thicknesses were measured from ECCI images and corrected values were then determined by means of a stereological correction considering the corresponding tilting conditions. Fig. 10a and b reveals that these crystals contain a refined dislocation substructure, consisting of HDDW structures and DCs with an average size of 550 nm at 0.3 true strain. With further deformation (0.4 true strain), the structure is refined to an average value of 450 nm. Fig. 10 also reveals that the dislocation–twin interaction is similar to that occurring in type II grains. As a consequence, a rhomboid-shaped nanostructure of twin boundaries and dislocation walls (HDDWs or cell walls) is formed. The evolution of this nanostructure is further favored by twin–twin intersections due to the activation of multiple twin systems.

4. Discussion

4.1. Evolution of the dislocation and twin substructure

Two important aspects of the substructure evolution during tensile testing are quantitatively examined in this study, namely the dislocation and twin substructures. As

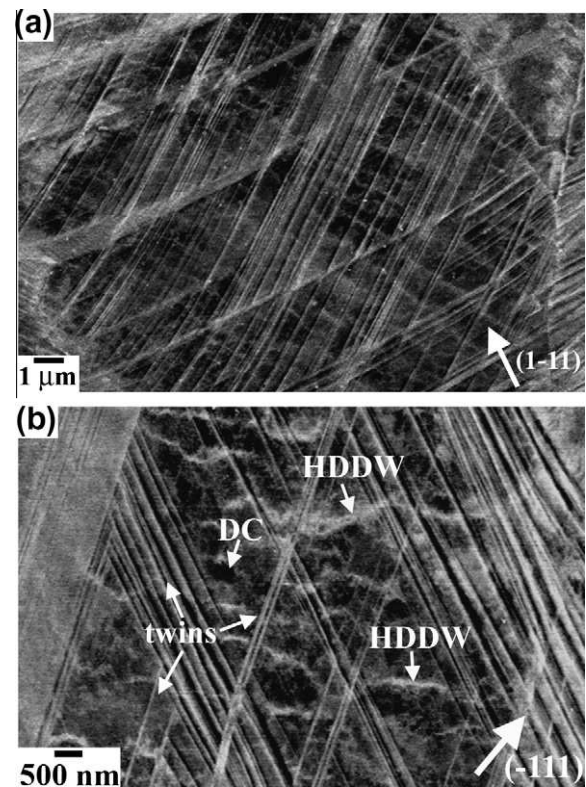


Fig. 10. ECCI images of deformation microstructure of a type III grain at 0.3 true strain. (a) Large field of view image showing a multiple twin structure with dislocation substructures. The ECCI image was obtained by orienting the grain into Bragg condition using the $(1\ -1\ 1)g$ vector (arrow). (b) Details of the dislocation substructure consisting of HDDWs and DCs. The ECCI image was obtained by orienting the grain into Bragg condition using the $(-1\ 1\ 1)g$ vector (arrow).

the ECCI images quantitatively reveal, during the early stages of deformation (strain below 0.1 true strain) the deformed microstructure is formed by DCs and highly dense dislocation arrangements (HDDWs and HDDW structures). ECCI images reveal dislocation patterns that are similar to those found in TEM observations on dislocation substructures in low-to-medium stacking fault energy metals [30–33]. In particular, the characteristic dislocation cell pattern observed by ECCI in the present FeMn alloy was confirmed by TEM in a previous work [24]. The dislocation substructures can be classified according to the character of the observed slip patterns, namely wavy or planar. The planar slip character in fcc metals is known to be mainly promoted by decreasing stacking fault energy, increasing friction stress and the occurrence of short-range ordering [35,36]. In the present TWIP steel, where ordering has not been observed, the two parameters that can promote planar slip are predominantly the friction stress ($\sigma_0 = 157$ MPa [17], which is higher than for materials exhibiting planar slip such as stainless steels [37,38]) and the stacking fault energy (22 mJ m^{-2} [39]). The latter effect promotes slip via Shockley partial dislocations. These can only cross-slip after stress- and thermally assisted local recombination, hence the planar slip prevalence in

materials with low stacking fault energy. With increasing strain (strain above 0.3 true strain), planar dislocation structures are further developed in grains that are characterized by a limited number of active slip systems, i.e. type II and III grains. Wavy dislocation structures are promoted in grains when a high number of slip planes are activated and dislocation cross-slip is enabled [30,40], such as in type I grains. Interestingly, in high stacking fault energy metals, such as pure aluminum, a similar crystallographic orientation dependence of the dislocation substructure was observed, as in the present Fe–Mn alloy [41]. This finding suggests that dislocation cell formation is promoted in similar crystal orientations in both low and high stacking fault energy metals, although the characteristic mechanism of cell formation may well be different, as discussed below. Regarding the formation of HDDWs in type III grains, the slip trace analysis conducted in 10 grains through combined ECCI and EBSD analysis reveals that most of the HDDWs are boundaries with a specific crystallographic orientation. Fig. 11a shows an example of HDDWs lying along two slip systems. The simulated diffraction pattern of the crystallographic orientation obtained from EBSD is shown in Fig. 11b. The grain is oriented close to the $(3\ -1\ -2)$ direction. Trace analysis reveals that the two sets

of HDDWs are formed with a specific crystallographic orientation. One set of HDDWs is formed along the $(1\ -1\ 1)$ slip plane. The other set is formed along the $(1\ -1\ -1)$ slip plane within a range of 10° . The present observations on HDDWs agree with previous results obtained in low stacking fault energy alloys, such as Hadfield steel [33,34]. Our result suggests that in type III grains there are two active slip systems in the same slip plane that account for a large fraction of the total slip in the respective crystal [42].

In a previous work [6], we have shown that in the present alloy, when tensile deformed to a high true strain of 0.3, only grains with either a highly favorable or unfavorable orientation for twinning follow the Schmid behavior. These grains correspond to crystals oriented close to the $\langle 1\ 1\ 1 \rangle // TA$ and $\langle 0\ 0\ 1 \rangle // TA$ directions, respectively. This result indicates that in the present twin substructure only type III and I grains follow the Schmid behavior. The rest of the crystals, viz. type II grains with a lamellar twin structure, do not fulfill Schmid's law when considering the macroscopic load. We also observe that local stress concentrations at grain boundaries (e.g. those caused by the impingement of deformation twins formed in a neighboring grain on a grain boundary) can promote twinning in unfavorably oriented grains. These stresses can be high enough to activate the twin system with the highest Schmid factor (primary twin system). The developed twin substructure may hinder the growth of deformation twins on secondary twin systems because the stress required to build up a secondary twin substructure is probably too high to be attained during tensile deformation. As a consequence, only primary deformation twin is activated, resulting in a lamellar twin structure. This effect is similar to the well-known effect of overshooting in slip due to latent hardening.

It is worth noting the relatively small mechanical resistance that dislocation boundaries (cell walls and HDDWs) have against twin boundaries that cut through them. If we consider that the interaction is stress controlled, this observation indicates that dislocation boundaries have a small influence on the stress required for twin dislocations to pass through them. This is supported by the fact that mechanical twins, once nucleated, practically always penetrate grains to the opposite grain boundary. This behavior can be discussed in terms of the self-stresses that characterize the leading twin edge. Mechanical twins in fcc metals are formed by the passage of edge-type Shockley partial dislocations on successive twinning planes. These partials form inclined arrays at the twin–matrix interface. Therefore, a twin can be described by a field of discrete partial dislocations where the long-range field resembles that of a pile-up configuration of partials [43–45]. Kamat et al. [44] have shown that under usual deformation conditions a twin resembles a discontinuous tilt wall formed by inclined pile-ups. This means that a growing twin can be considered as a coordinated movement of partial dislocations that preserve their characteristic arrangement. The partial dislocations in this array are spaced by a value of h (Fig. 12a). The

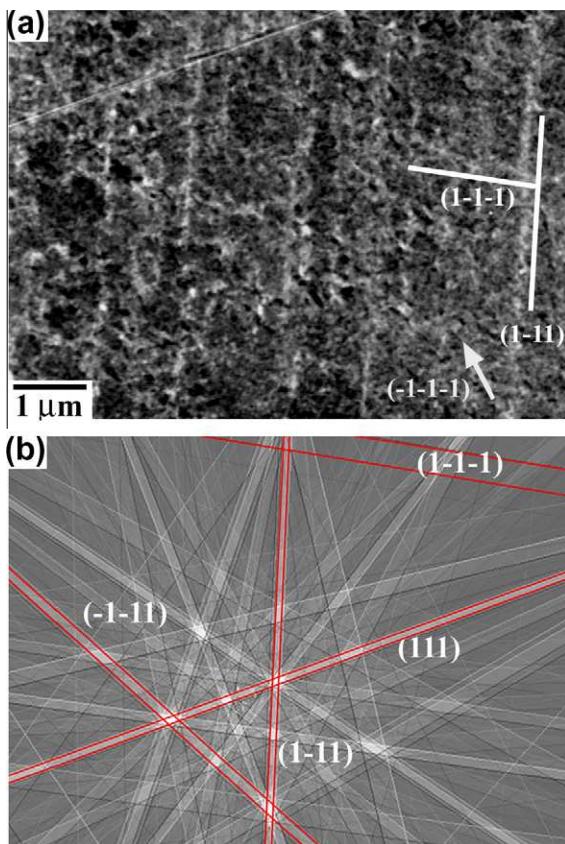


Fig. 11. Trace analysis of the crystallographic orientation of the alignment of HDDWs by using a combination of ECCI and EBSD. (a) ECCI image of HDDWs. (b) Simulated diffraction pattern of the corresponding crystal orientation. The crystal orientation is close to the $(3\ -1\ -2)$ direction//TA.

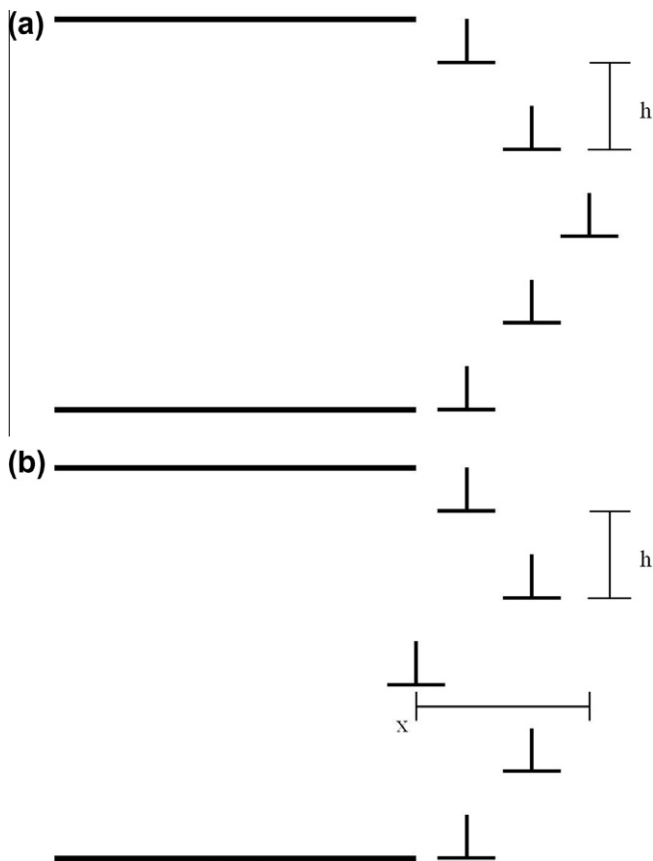


Fig. 12. Schematic representation of the leading edge of a deformation twin formed by a set of Shockley partials separated by distance h . (a) Twin tip in local mechanical equilibrium. (b) Twin tip out of local mechanical equilibrium with the leading partial dislocation being retarded and displaced by x . The local Peach–Koehler forces on this dislocation are in the GPa range, so the local mechanical equilibrium will push such a retarded dislocation back into the array against the obstacle force (such as from a forest interaction).

collective and highly coordinate movement of partial dislocations can be driven, for example, by screw dislocation poles [46,47]. We suggest that the required highly coordinate slip of partials is the reason for the relatively unimpeded penetration of deformation twins through existing dislocation arrangements compared to an equivalent set of partial dislocations in non-coordinated motion. When one of the partials is retarded due to a forest dislocation interaction between the twin tip and the dislocation substructure in front of it, and thus deviates from its ideal position within the twin tip, the local Peach–Koehler force by the other partials assembled in the twin tip array becomes very high and pushes it back into the required dislocation configuration. For example, the force, F , on the displaced partial dislocation (displacement, x) of the twin tip depicted in Fig. 12b due to partials of the twin tip array can be considered as the force provided by two superdislocations having a magnitude Nb , where N is the number of dislocations in the twin tip array and b is the Burgers vector. Accordingly, the force F can be written as: $F/b \sim GbN/x\pi(1-\nu) + \gamma$, where G is the shear modulus, ν is the

Poisson ratio, N is the number of dislocations in the twin tip array and γ is the stacking fault energy. Assuming a displacement x of the Burgers vector b , the force is: $F/b \sim GN/\pi(1-\nu) + \gamma$. This force is much higher than the self-stress field of a dislocation boundary or the back-driving force created by a forest reaction product [48], and consequently the trailing partial is pushed back to its position within the twin tip.

4.2. Scaling law for dislocation cell sizes

Fig. 13 shows the variation in average size of dislocation substructures with true stress in type I and type III grains. The figure reveals that the refinement in the dislocation substructure in type III grains (HDDW structures and DCs) is less significant than that observed in type I grains (DCs). This is attributed to the activation of twinning in type III grains. As slip and twinning are two competing deformation mechanisms, the strain accommodated by slip is remarkably reduced and therefore the dislocation substructure is less refined. The figure also reveals that the variation in average size of the DCs in type I grains follows the relationship $\sigma = k/D$, where σ is the true stress, k is a constant and D is the cell size. This is a widely observed empirical relationship that has been established in the framework of the mesh-length theory of work hardening [40]. According to this theory, dislocations tend to arrange into structures which minimize the elastic energy per unit length of the dislocation line (low energy dislocation configurations). One characteristic substructure type of arrangement, viz. dislocation cell formation, minimizes the elastic energy per unit length of dislocation line through this relationship. In particular, the following relationship between the flow stress and the cell size has been proposed for cell-forming metals [40], and is known as the “similitude principle”:

$$\tau = \tau_0 + KGb/D \quad (1)$$

where τ is the flow stress, τ_0 is the friction shear stress, K is the similitude constant, G is the shear modulus, b is the Burgers vector and D is the cell size. Fig. 14 shows relation

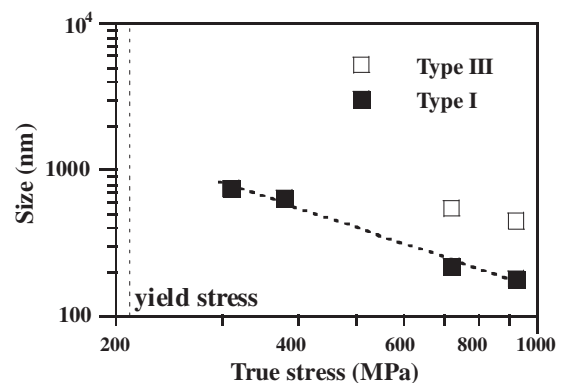


Fig. 13. Variation of the average size of the dislocation substructure with the true stress in type I grains (DCs, black symbols) and type III grains (dislocation cells plus HDDW structures, open symbols).

(1) for the present TWIP steel using $\sigma_0 = 157$ MPa [17], $b = 2.5 \times 10^{-10}$ m [15] and $G = 65$ GPa [15]. τ was obtained from σ assuming a Schmid factor m of 0.41, which corresponds to $\langle 001 \rangle // TA$ orientations. From this diagram a value for the constant K of 3.7 is obtained. This value is smaller than the commonly reported value for fcc metals (medium-to-high stacking fault energy metals), which ranges between 7 and 8 [49]. Although there are few studies on dislocation cell kinetics in low stacking fault energy alloys, a small value of the constant K between 2.0 and 2.9 has been reported for 316 L austenitic stainless steel [49,50], which is close to that obtained in the present study.

According to the mesh-length theory of work hardening, any fcc metal should develop a dislocation cell structure, according to the criterion:

$$10^2 \leq G/(\tau - \tau_0) \leq 10^5 \quad (2)$$

where G is the shear modulus, τ is the resolved shear stress and τ_0 is the friction stress. For the present steel, the term $G/(\tau - \tau_0)$ ranges between 1.7×10^2 and 1×10^3 , hence a dislocation cell structure is formed. However, it must be noted that this theory only accounts for dislocation cell formation on the basis of a low energy configuration criterion; it does not provide any detail on the kinetic mechanism of cell formation. Several observations revealed that dislocation cell formation is closely connected with the cross-slip ability of screw dislocations [48,51]. Cross-slip plays an important role in this process through the rearrangement of screw dislocations in terms of the activation of secondary slip and annihilation of screw dislocations of opposite sign. The localized maneuvers of partial dislocations to transfer dislocation screw segments from one plane to a cross-slip plane depends on the stacking fault energy [48,51]. Consequently, the stacking fault energy has an important influence on the characteristic mechanism of dislocation cell formation. For this reason, the mechanism of cell formation in the present TWIP steel may be different to that occurring in medium-to-high stacking fault energy

metals and therefore a different similitude constant K is obtained. Similar observations were recently reported in copper [49]. The material had been strained by cyclic deformation and a similar constant to that in the present study was found [49]. In their work, the authors attributed the low value of the similitude constant K to a higher storage rate of dislocations when compared to monotonic deformation. Although this aspect, viz. the high dislocation density, must also be taken into account in low stacking fault energy alloys due to the reduced activity of dislocation cross-slip, its effect on the mechanism of dislocation cell formation is not clear.

4.3. Strain hardening

Strain hardening of the Fe–22 wt.% Mn–0.6 wt.% C TWIP steel is characterized by a remarkably high strain hardening above a true stress of 270 MPa. Microstructure observations conducted by ECCI confirm that this is attributed to both dislocation accumulation and twin substructure formation.

Stage A hardening in the present alloy is characterized by a decrease in the strain hardening rate. It reveals similar features to the conventional stage III hardening regime observed in high stacking fault energy metals [28], and also agrees with previous studies on strain hardening of low stacking fault energy metals [52]. This observation suggests that this stage can be attributed to the prevalence of dynamic recovery processes, such as cross-slip and annihilation of screw dislocations of opposite signs. The microstructure observations indicate that stage B hardening, which is characterized by a constant strain hardening rate with a hardening coefficient of about $G/40$, can be attributed to the evolution of the dislocation substructure consisting of DCs and HDDW structures. The value of the strain hardening coefficient observed in this regime is much higher than the typical value of $G/200$ observed for multiple slip in common fcc metals [28] but is similar to that reported for Hadfield steels ($G/20$ – $G/30$ [33,34]). These alloys contain dislocation arrangements organized in HDDWs that act as effective obstacles against dislocation motion. Some portion of the blocked dislocations can become trapped by the boundaries, thereby increasing their dislocation density (i.e. the wall thickness). In the present alloy the presence of weaker obstacles (DCs) may result in less strain hardening. The present study hence shows for the first time the important effect of dislocation substructures on the strain hardening behavior in a TWIP steel.

The development of a dense twin substructure upon ongoing straining results in a further drastic decrease in the MFP. Consequently, strain hardening increases up to a hardening coefficient of about $G/30$, leading to stage C hardening. The microstructure observations reveal that twin boundaries cut through the existing dislocation substructure, resulting in further microstructure refinement. Twin boundaries act as strong obstacles to dislocation

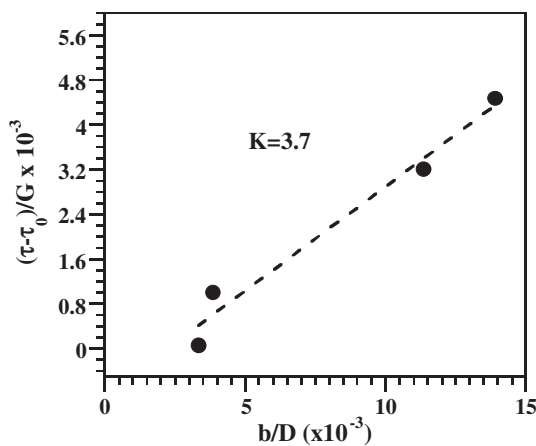


Fig. 14. Plot of the relation $(\tau - \tau_0)/G = Kb/D$ for average dislocation cell sizes in type I grains.

motion, serving as efficient sites for dislocation accumulation similar to grain boundaries. This effect is referred to as a “dynamic Hall–Petch effect”, and has been reported in many fcc metals containing deformation twins [3,15,16,52,53].

To obtain a better understanding of the influence of both dislocation and twin substructures to stage C hardening, we evaluate the contribution of the different types of grains (types I, II and III) to the flow stress at 0.3 true strain using an MFP approach. This strain level corresponds to the onset of stage D, where the highest strain hardening is obtained. The contribution of type I grains (cell forming grains) to the flow stress is provided by relation (1). Type II grains develop a block structure formed by twin boundaries and dislocation boundaries. As the average twin spacing is around half the average spacing between dislocation boundaries, we consider the average twin spacing to be the dominant microstructural correlation length in the overall MFP for mobile dislocations. Accordingly, we assume that the contribution of type II grains to the flow stress can be described in terms of a Hall–Petch-type relation [52]:

$$\sigma = \sigma_0 + K_{H-P}/(\lambda_{\text{twin}})^{1/2} \quad (3)$$

where σ_0 is the friction stress, K_{H-P} is the Hall–Petch constant for twinning and λ_{twin} is the average twin spacing. Type III grains develop a block structure formed by twin and dislocation boundaries (HDDWs and cell walls). As a first approximation, we consider only the smallest obstacle spacing, which is the average twin spacing of one of the active twinning system. We therefore assume that the contribution of type III grains to the flow stress is also provided by relation (3), with λ_{twin} being the smallest average twin spacing of the active twin system. Considering these three contributions, the expression for the flow stress can be written as:

$$\sigma = \sigma_0 + f_I G K b M / D + f_{II} K_{H-P} / (\lambda_{\text{twin}}^{II})^{1/2} + f_{III} K_{H-P} / (\lambda_{\text{twin}}^{III})^{1/2} \quad (4)$$

where σ_0 is the friction stress, f_I , f_{II} and f_{III} are the area fractions of type I, II and III grains, respectively, G is the shear modulus, b is the Burgers vector, K is a constant, M is the Taylor factor, D is the average cell size, K_{H-P} is the Hall–Petch constant for twinning, $\lambda_{\text{twin}}^{II}$ is the average twin spacing in type II grains, and $\lambda_{\text{twin}}^{III}$ is the smallest average twin spacing of an active twin system in type III grains. The area fraction, average size of dislocation substructures and average twin spacing of each type of grain are shown in Table 1. Assuming $\sigma_0 = 157$ MPa [17], $b = 2.5 \times 10^{-10}$ m [15], $G = 65$ GPa [15], $K = 3.7$ (calculated in the previous section), $M = 2.44$ (Taylor factor for type I grains) and $K_{H-P} = 357$ MPa $\mu\text{m}^{1/2}$ [17] (a previous work has shown that in the present TWIP steel the Hall–Petch constant for twinning is similar to that for slip [6]), and taking the microstructure parameters shown in Table 1, yields a flow

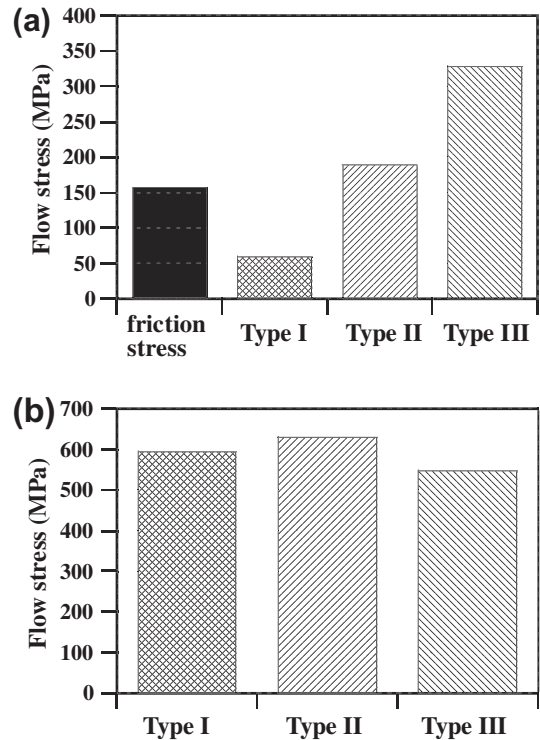


Fig. 15. (a) Contribution of the friction stress and type I, II and III grains to the flow stress at 0.3 true strain. (b) Intrinsic strength of type I, II and type III grains at 0.3 true strain. Type I grains: equiaxed cell structure with a low deformation twinning activity; type II grains: well-developed twin substructure along one active twinning system (primary twin system); type III grains: DCs and HDDW structures with a well-developed twin substructure along more than one active twinning system (primary and secondary twin systems) (see also Fig. 7 and Table 1).

stress of 735 MPa at 0.3 true strain. This value is close to the experimentally observed flow stress value of 720 MPa.

Two important findings can be drawn from this estimate. First, the strain hardening of a TWIP steel can be analyzed in terms of the MFP approach. This result agrees with published models on the hardening behavior of TWIP steels [13,14,17]. Second, we have identified the different microstructure parameters controlling strain hardening in this material, namely, the average dislocation cell size in type I grains, the average twin spacing in type II grains and the smallest average twin spacing of the active twin system in type III grains. Fig. 15a shows the contribution to the flow stress of each term occurring in relation (4). The figure reveals that the most significant contribution to the flow stress is provided by the twin substructure (type II and III grains) with about 70% contribution to the overall flow stress. In particular, type III crystals, which are the most frequently occurring grains, provide the highest contribution. Interestingly, the contribution of the dislocation substructure, which is mainly provided by type I grains, is still noticeable, with about 8% of the flow stress. This analysis clarifies the influence of the main microstructure features, namely dislocation and twin substructures, on the high strain hardening rate of TWIP steels. It shows that the high strain hardening rate observed in stage C is mainly attributed to the MFP refinement due to deformation

twinning in type II and III grains. If we only consider the intrinsic strength of each type of grain, we find that type II crystals (with a lamellar twin structure) are the hardest grains (Fig. 15b). Interestingly, this figure reveals that at this deformation stage type I grains (cell forming grains) exhibit an even higher strength than type III grains (multiple twin structure). This result supports the previous finding of the significant contribution of dislocation substructures on strain hardening in the present TWIP steel.

With further straining, the refinement of the twin spacing proceeds, leading to a further reduction in the dislocation MFP and a gradual decrease in the strain hardening rate. The hardening coefficient of stage D is still high ($G/30$), indicating the gradual refinement of the MFP, as also revealed by Table 1. Above a true stress of 800 MPa, in stage E, strain hardening steadily decreases, indicating the reduced capability for trapping more dislocations inside the refined microstructure. The work hardening capability is determined not only by the MFP but also by the specific strengthening effect of the deformation twins when they act as obstacles against dislocation motion. In the present FeMn alloy, deformation twins are arranged in bundles. Microstructure observations reveal that the bundle density and thickness increase gradually with strain. This indicates that the number of deformation twins arranged in bundles increases with the strain as well. These bundles are even stronger obstacles to dislocation glide than single twins because the critical stress required to carry plastic deformation across the twin bundle is much higher than that required to penetrate a single twin due to the small interface spacing. Another result supporting the increasing twin strength with deformation is the high density of sessile dislocations found within twin lamellae in an Fe–20 wt.% Mn–1.2 wt.% C TWIP steel [7,18]. The accumulation of sessile dislocations within the twin is attributed to dislocation reactions between Shockley partials and twin dislocations. These sessile dislocations are potential obstacles to dislocation motion and can provide not only a hardening mechanism within deformation twins but also an increase in the critical stress required to induce plastic deformation across the twin as well. Furthermore, in the present TWIP steel, Shockley partial-twin dislocation interactions can be enhanced by the interaction between HDDWs and cell boundaries with twin boundaries. Accordingly, we suggest that, in the present TWIP steel, deformation twins contain a high dislocation density as well. As the dislocation density is increased by dislocation storage through interactions, the dislocation density will increase with further deformation. These two aspects associated with the role of deformation twins, namely the arrangement in twin bundles and the high dislocation density within them, increase the stress required to transfer plastic deformation across deformation twins and therefore limit the further work hardening capacity at high strains in this material.

5. Conclusions

We have investigated the underlying defect topology and kinetics of substructure evolution and its correspondence to the strain hardening evolution of an Fe–22 wt.% Mn–0.6 wt.% C TWIP steel during tensile deformation by means of ECCI and EBSD. We draw the following conclusions:

- At the early stages of plastic deformation (below 0.1 true strain), the microstructure consists of dislocation cells and highly dense dislocation arrangements. These dislocation substructures are strong barriers to dislocation glide and result in a high strain hardening with a hardening coefficient of about $G/40$. This result underlines the importance of dislocation substructures at the early stages of strain hardening in TWIP steels.
- At intermediate strains (0.1–0.3 true strain), a well-defined deformation twin substructure is developed. Twinning depends on the crystallographic grain orientation. We classify the microstructure in this regime according to its twin substructure into three groups, referred to as types I, II and III. We quantify strain hardening in terms of a dislocation mean free path approach. The different microstructure parameters controlling strain hardening in this regime are: the average dislocation cell size in type I grains; the average twin spacing in type II grains; and the smallest average twin spacing of an active twin system in type III grains. The analysis shows that the refinement in the dislocation mean free path due to deformation twinning in type II and III grains results in a high strain rate with a hardening coefficient of about $G/30$.
- At high strains (above 0.4 true strain), the reduced further refinement of the dislocation and twin substructure together with the increasing strengthening effect of the individual deformation twins as obstacles to dislocation glide reduce the capability for trapping more dislocations, hence the strain hardening decreases.
- The cell structure formed in type I grains follows the similitude principle $\tau = \tau_0 + KGb/D$ with a similitude constant of $K = 3.7$. This value is smaller than the value of 7–8 that is typically observed in medium-to-high stacking fault alloys. We attribute this difference to the influence of the stacking fault energy on the mechanism of cell formation.

Acknowledgements

The authors would like to acknowledge the financial support by the German Research Foundation (Deutsche Forschungsgemeinschaft DFG) within the framework of the SFB 761 “steel ab initio”.

References

- [1] Grässel O, Krüger L, Frommeyer G, Meyer LW. *Int J Plast* 2000;16:1391.
- [2] Lü Y, Hutchinson B, Molodov DA, Gottstein G. *Acta Mater* 2010;58:3079.
- [3] Jin JE, Lee YK. *Mater Sci Eng A* 2009;527:157.
- [4] Kim JK, Chen L, Kim HS, Kim SK, Estrin Y, Cooman BCD. *Metall Mater Trans A* 2009;40:3147.
- [5] Curtze S, Kuokkala VT. *Acta Mater* 2010;58:5129.
- [6] Gutierrez-Urrutia I, Zaefferer S, Raabe D. *Mater Sci Eng A* 2010;527:3552.
- [7] Idrissi H, Renard K, Schryvers D, Jacques PJ. *Scripta Mater* 2010;63:961.
- [8] Lü Y, Molodov DA, Gottstein G. *Acta Mater* 2011;59:3229.
- [9] Yoo JD, Park KT. *Mater Sci Eng A* 2008;496:417.
- [10] Yoo JD, Hwang SW, Park KT. *Metall Mater Trans A* 2009;40:1520.
- [11] Olson GB, Cohen M. *Metall Trans A* 1976;7:1897.
- [12] Olson GB, Cohen M. *Metall Trans A* 1976;7:1905.
- [13] Allain S, Chateau JP, Bouaziz O. *Mater Sci Eng A* 2004;387–389:143.
- [14] Shiekhsouk MN, Favier V, Inal K, Cherkaoui M. *Int J Plast* 2009;25:105.
- [15] Bouaziz O, Allain S, Scott C. *Scripta Mater* 2008;58:484.
- [16] Barbier D, Gey N, Allain S, Bozzolo N, Humbert M. *Mater Sci Eng A* 2009;500:196.
- [17] Sevillano JG. *Scripta Mater* 2009;60:336.
- [18] Idrissi H, Renard K, Ryelandt L, Schryvers D, Jacques PJ. *Acta Mater* 2010;58:2464.
- [19] Ng BC, Simkin BA, Crimp MA. *Mater Sci Eng A* 1997;239–240:150.
- [20] Wilkinson AJ, Hirsch PB. *Micron* 1997;28:279.
- [21] Ng BC, Simkin BA, Crimp MA. *Ultramicroscopy* 1998;75:137.
- [22] Ahmed J, Roberts SG, Wilkinson AJ. *Philos Mag* 2006;86:4965.
- [23] Crimp MA. *Microsc Res Tech* 2006;69:374.
- [24] Gutierrez-Urrutia I, Zaefferer S, Raabe D. *Scripta Mater* 2009;61:737.
- [25] Weidner A, Martin S, Klemm V, Martin U, Biermann H. *Scripta Mater* 2011;64:513.
- [26] Senk D, Emmerich H, Rezende J, Siquieri R. *Adv Eng Mater* 2007;9:695.
- [27] Raabe D, Sachtleber M, Zhao Z, Roters F, Zaefferer S. *Acta Mater* 2001;49:3433.
- [28] Kocks UF, Mecking H. *Prog Mater Sci* 2003;48:171.
- [29] Ueji R, Tsuchida N, Terada D, Tsuji N, Tanaka Y, Takemura A, et al. *Scripta Mater* 2008;59:963.
- [30] Bay B, Hansen N, Hughes DA, Kuhlmann-Wilsdorf D. *Acta Metall Mater* 1992;40:205.
- [31] Hansen N. *Scripta Metall Mater* 1992;27:1447.
- [32] Hansen N, Jensen DJ. *Philos Trans Roy Soc* 1999;357:1447.
- [33] Canadinc D, Sehitoglu H, Maier HJ, Chumlyakov YI. *Acta Mater* 2005;53:1831.
- [34] Canadinc D, Sehitoglu H, Maier HJ. *Mater Sci Eng A* 2007;454–455:662.
- [35] Gerold V, Karnthaler HP. *Acta Metall* 1989;37:2177.
- [36] Hong SI, Laird C. *Acta Metall Mater* 1990;38:1581.
- [37] Kassner ME, Miller AK, Sherby OD. *Metall Trans A* 1982;13:1977.
- [38] Lo KH, Shek CH, Lai JKL. *Mater Sci Eng R* 2009;65:39.
- [39] Bracke L, Kestens L, Penning J. *Scripta Mater* 2009;61:220.
- [40] Kuhlmann-Wilsdorf D. *Mater Sci Eng A* 1989;113:1.
- [41] Hansen N, Huang X. *Acta Mater* 1998;46:1827.
- [42] Winther G, Jensen DJ, Hansen N. *Acta Mater* 1997;45:5059.
- [43] Mitchell TE, Hirth JP. *Acta Metall Mater* 1991;39:1711.
- [44] Kamat SV, Hirth JP, Müllner P. *Philos Mag A* 1996;73:669.
- [45] Müllner P, Solenthaler C, Speidel MO. *Acta Metall Mater* 1994;42:1727.
- [46] Christian JW, Mahajan S. *Prog Mater Sci* 1995;39:1.
- [47] Niewczas M. In: Nabarro FRN, Hirth JP, editors. *Dislocations in solids*, vol. 13. Amsterdam: Elsevier B.V.; 2007.
- [48] Hirth JP, Lothe J. *Theory of dislocations*. 2nd ed. New York: John Wiley and Sons; 1982.
- [49] Sauzay M, Kubin LP. *Prog Mater Sci* 2011;56:725.
- [50] Feaugas X. *Acta Mater* 1999;47:3617.
- [51] Jackson PJ. *Prog Mater Sci* 1985;29:139.
- [52] Asgari S, El-Danaf E, Kalidindi SR, Doherty RD. *Metall Mater Trans A* 1997;28:1781.
- [53] Karaman I, Sehitoglu H, Maier HJ, Chumlyakov YI. *Acta Mater* 2001;49:3919.